

Supporting Information

To

How does a single Pt nanocatalyst behave in two different reactions? A single-molecule study

*Kyu Sung Han, Guokun Liu, Xiaochun Zhou, Rita E. Medina, Peng Chen**

Department of Chemistry and Chemical Biology, Cornell University, Ithaca, New York 14853, USA

1. Materials and Methods

1.1. Materials. All chemicals were used as received from vendors, unless specified otherwise.

1.2. Pt nanoparticles synthesis. Pt nanoparticles (Pt NPs) of 4.6 ± 0.9 nm in diameter were prepared by the reduction of chloroplatinic acid hexahydrate ($\text{H}_2\text{PtCl}_6 \cdot (\text{H}_2\text{O})_6$, Sigma-Aldrich) in aqueous solution that also contains citrate ions according to reference.¹ 36 mL of a 0.2% solution of $\text{H}_2\text{PtCl}_6 \cdot (\text{H}_2\text{O})_6$ was added into 464 mL boiling deionized water and kept boiling and stirring for 1 min. Then 11 mL of a solution containing 1% sodium citrate and 0.05% citric acid was added. After 30 s, 5.5 mL of 0.08% sodium borohydride solution containing 1% sodium citrate and 0.05% citric acid was quickly injected. The obtained solution was kept boiling and stirring for 10 min and then cooled down to room temperature.

1.3. Single-molecule fluorescence imaging of single nanoparticle catalysis. For single-molecule fluorescence measurements, 100 μL of ~ 1 nM colloidal Pt nanoparticle solution was drop-casted on a quartz slide and dried for 30 min in air. The quartz slide was then assembled into a microfluidic channel (3 cm \times 5 mm \times 100 μm , length \times width \times height) using a cover slip and a double-sided tape as a spacer. Two holes were drilled on the quartz slide to connect to polyethylene tubing for supplying the reactant solution driven by a syringe pump. The flow channel was flushed intensively several times to remove weakly bound Pt nanoparticles on the slide, before single-molecule imaging experiments were performed. The reactions were carried out at a 10 $\mu\text{L}/\text{min}$ flow rate containing 0.3–10 μM amplex red and 200 mM H_2O_2 for the oxidative *N*-deacetylation reaction, or containing 0.001–1 μM resazurin and 0.025–8 mM N_2H_4 for the reductive *N*-deoxygenation reaction; both in aqueous solutions and at room temperature.

Single-molecule fluorescence imaging was performed on a prism-type total internal reflection (TIR) fluorescence microscope based on an Olympus IX71 inverted microscope. A continuous wave circularly polarized 532 nm laser beam of ~ 6 mW was focused onto the sample to directly excite the fluorescence of the product resorufin. The fluorescence signal was collected by a 60X NA1.2 water-immersion objective (UPLSAPO60XW, Olympus), filtered by two filters (HQ550LP, HQ580m60), and projected onto a camera (Andor iXon EMCCD), which was controlled by an Andor IQ software, with 20 ms frame rate. The recorded fluorescence movies were analyzed using a home-written IDL program, which extracted the fluorescence intensity trajectories from localized fluorescence spots individually

across the entire movie. The intensity of each fluorescence spot in an image was obtained by integrating the signal counts over an area of $\sim 1 \times 1 \mu\text{m}^2$; the background signal was subtracted.

1.4. Purification of resazurin. To suppress maximally the background noise, commercial resazurin (Invitrogen), which contains $\sim 4\%$ resorufin contamination, was further purified by thin layer chromatography (TLC). The amount of resorufin was estimated by its solution fluorescence band at $\sim 580 \text{ nm}$ (Figures S1), calibrated to solutions of known resorufin concentrations. TLC was performed on a sheet of aluminum foil coated with a thin layer of silica. The solvent was a mixture of CH_3CN , CHCl_3 and CH_3OH with a ratio of 9:1:1. The purified resazurin by TLC process contains $\sim 0.14\%$ resorufin, as shown in Figure S1.

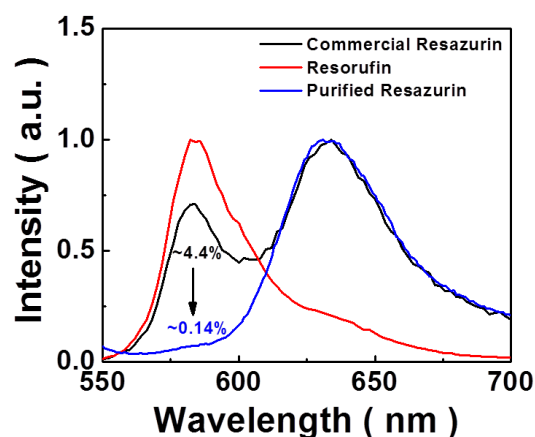


Figure S1. Fluorescence spectra of the commercial and purified resazurin at pH 7.4, 1 mM phosphate buffer. The fluorescence spectrum of resorufin is shown as well for comparison. All spectra were normalized to have maximum intensity of 1 (arbitrary units). The fluorescence band at $\sim 640 \text{ nm}$ is the weak fluorescence signal of resazurin; the band at $\sim 580 \text{ nm}$ is that of resorufin.

1.5. Other measurements. The size distribution and morphology of the Pt NPs were characterized by transmission electron microscopy (TEM, FEI Tecnai 12) at the Cornell Center for Materials Research. Ensemble catalytic properties of Pt NPs were studied using UV-Vis absorption (Beckman Coulter, DU 800 spectrophotometer) or fluorescence (Agilent Eclipse fluorometer). NMR (INOVA 600, Oxford) was used to identify the products of Pt-nanoparticle-catalyzed *N*-deacetylation reaction. The NMR samples were prepared in aqueous solution (5:1 $\text{H}_2\text{O}:\text{D}_2\text{O}$); DMSO (2.71 ppm) was used as an internal standard for chemical shift.

2. Derivation of the probability density function $f(\tau)$ of the microscopic reaction time τ , and of $\langle \tau \rangle^{-1}$ for a nanoparticle-catalyzed reaction that follows Langmuir-Hinshelwood mechanism with two reactants.

We considered the Langmuir-Hinshelwood mechanism for heterogeneous catalysis for analyzing the reaction kinetics of both the oxidative *N*-deacetylation reaction of amplex red to resorufin and the reductive *N*-deoxygenation reaction of resazurin to resorufin. Both these two reactions involve two reactant molecules. The Langmuir-Hinshelwood mechanism assumes:²

(i) The sites of each reactant binds are uniform on each nanoparticle. In reality, there are different surface sites on each nanoparticle. However, our measurements do not differentiate reactions on different sites on a single particle, and thus the single-particle kinetic parameters we obtained are averaged properties of the many sites on *each particle*. The assumption of uniform sites is thus a valid approximation within our experimental limitation.

(ii) Quasi-equilibrium in adsorption of reactants on surface sites (i.e., reactant molecules bind to the nanoparticle surface reversibly and fast adsorption equilibrium is established at all times). The surface coverage of reactant molecules is determined by the Langmuir isotherm.

(iii) Rapid dissociation of the product molecules from the nanoparticle surface, as compared with the rate of catalytic conversion. This assumption is consistent with our experimental observation that the duration of the fluorescence bursts, which is the dwell time of the product molecule on the nanoparticle, is very short compared with the time separation between fluorescence bursts (Figure 1D).

Based on this mechanism, the kinetic scheme that involves two reactant molecules is:



Here M stands for a nanoparticle; n and l the numbers of reactants A and B adsorbed on the nanoparticle surface, respectively; P stands for the product. k_{app} is the apparent rate constant for forming one product on the surface of one nanoparticle. From Langmuir-Hinshelwood kinetics for heterogeneous catalysis, k_{app} takes the form:²

$$k_{\text{app}} = knl \quad (\text{S1})$$

Here k is a rate constant. n and l are the numbers of A and B molecules adsorbed at the catalytic sites on the surface of a single nanoparticle, respectively.

If the two reactants adsorb to different types of surface sites (i.e., non-competitive adsorption), Langmuir adsorption equilibrium gives:²

$$n = n_{\text{TA}}\theta_A = n_{\text{TA}} \frac{K_A[\text{A}]}{1 + K_A[\text{A}]} \quad (\text{S2})$$

$$l = n_{\text{TB}}\theta_B = n_{\text{TB}} \frac{K_B[\text{B}]}{1 + K_B[\text{B}]} \quad (\text{S3})$$

Here n_{TA} and n_{TB} are the total numbers of adsorption sites for the reactants A and B on one nanoparticle, respectively. θ_A and θ_B are the fractions of occupied A and B adsorption sites. K_A and K_B are the adsorption equilibrium constants of A and B.

If the two reactants adsorb to the same types of surface sites (i.e., competitive adsorption), the following relations apply:²

$$n = n_{\text{T}}\theta_A = n_{\text{T}} \frac{K_A[\text{A}]}{1 + K_A[\text{A}] + K_B[\text{B}]} \quad (\text{S4})$$

$$l = n_{\text{T}}\theta_B = n_{\text{T}} \frac{K_B[\text{B}]}{1 + K_A[\text{A}] + K_B[\text{B}]} \quad (\text{S5})$$

In conventional ensemble measurements where reactions of a large ensemble of nanoparticles are measured in solution simultaneously, the kinetic rate equations for Scheme 1 are:

$$\frac{d[\text{MA}_n\text{B}_l]}{dt} = -k_{\text{app}}[\text{MA}_n\text{B}_l] \quad (\text{S6})$$

$$\frac{d[\text{MA}_{n-1}\text{B}_{l-1} - \text{P}]}{dt} = k_{\text{app}}[\text{MA}_n\text{B}_l] \quad (\text{S7})$$

where $[\text{MA}_n\text{B}_l]$ is the concentration of the nanoparticles that do not carry any product, and $[\text{MA}_{n-1}\text{B}_{l-1} - \text{P}]$ is the concentration of nanoparticles on which one product molecule is generated.

Under conditions of single-nanoparticle measurements, although the concentrations of the reactants [A] and [B] in the surrounding solution are still valid descriptions, the concentration of one

nanoparticle is meaningless and needs to be replaced by the probability of the single nanoparticles. Then, Equations (S6) and (S7) turn to:

$$\frac{dP_{MA_nB_l}(t)}{dt} = -k_{app} P_{MA_nB_l}(t) \quad (S8)$$

$$\frac{dP_{MA_{n-1}B_{l-1}-P}(t)}{dt} = k_{app} P_{MA_nO_l}(t) \quad (S9)$$

where $P(t)$'s are the probabilities for finding a *single nanoparticle* in the states MA_nB_l and $MA_{n-1}B_{l-1}-P$ at a particular time t . At $t = 0$, no product molecule has formed. So the initial conditions for solving the equations are

$$P_{MA_nB_l}(0) = 1 \quad (S10)$$

$$P_{MA_{n-1}B_{l-1}-P}(0) = 0 \quad (S11)$$

and at any given time t ,

$$P_{MA_nB_l}(t) + P_{MA_{n-1}B_{l-1}-P}(t) = 1 \quad (S12)$$

We can then evaluate the probability density function $f(\tau)$ of the time τ required to complete the reaction in Scheme (1). The probability for finding a particular τ is $f(\tau)\Delta\tau$, which is equal to the probability of switching from the MA_nB_l state to the $MA_{n-1}B_{l-1}-P$ state for the nanoparticle between $t = \tau$ and $\tau + \Delta\tau$, which is $\Delta P_{MA_{n-1}B_{l-1}-P}(\tau)$. And, $\Delta P_{MA_{n-1}B_{l-1}-P}(\tau) = -\Delta P_{MA_nB_l}(\tau) = k_{app} P_{MA_nB_l}(\tau)\Delta\tau$. Therefore,

$$f(\tau) = \frac{dP_{MA_{n-1}B_{l-1}-P}(\tau)}{d\tau} = k_{app} P_{MA_nB_l}(\tau) \quad (S13)$$

Solving Equations (S8) and (S9) with the initial conditions for $P_{MA_nB_l}(\tau)$, we obtain:

$$f(\tau) = k_{app} \exp(-k_{app}\tau) \quad (S14)$$

And therefore, $\langle \tau \rangle^{-1}$, which represents the time-averaged product formation rate for a *single nanoparticle*, is:

$$\langle \tau \rangle^{-1} = 1 / \int_0^{\infty} \tau f(\tau) d\tau = k_{app} \quad (S15)$$

Combining Equations (S1)–(S5) and (S14)–(S15), we have: (i) for the case that the two reactants adsorb non-competitively:

$$f(\tau) = k_{eff} \frac{K_A K_B [A][B]}{(1 + K_A [A])(1 + K_B [B])} \exp(-k_{eff} \frac{K_A K_B [A][B]}{(1 + K_A [A])(1 + K_B [B])} \tau) \quad (S16)$$

$$\langle \tau \rangle^{-1} = k_{eff} \frac{K_A K_B [A][B]}{(1 + K_A [A])(1 + K_B [B])} \quad (S17)$$

Here $k_{eff} = kn_{T1}n_{T2}$, and k_{eff} represents the combined reactivity of all surface catalytic sites on one nanoparticle. Equations (S16) and (S17) are presented as Equations (3a) and (1a) in the main text with modifications on the symbols.

And (ii) for the case that the two reactants adsorb competitively:

$$f(\tau) = k_{eff} \frac{K_A K_B [A][B]}{(1 + K_A [A] + K_B [B])^2} \exp(-k_{eff} \frac{K_A K_B [A][B]}{(1 + K_A [A] + K_B [B])^2} \tau) \quad (S18)$$

$$\langle \tau \rangle^{-1} = k_{eff} \frac{K_A K_B [A][B]}{(1 + K_A [A] + K_B [B])^2} \quad (S19)$$

Here $k_{\text{eff}} = kn_T^2$, and k_{eff} again represents the combined reactivity of all surface catalytic sites on one nanoparticle. Equations (S18) and (S19) are presented as Equations (3b) and (2) in the main text with modifications on the symbols.

3. Ensemble measurements of Pt-nanoparticle-catalyzed reactions.

Prior to single-molecule experiment, we performed ensemble measurements to test the ability of the Pt nanoparticles in catalyzing both the oxidative *N*-deacetylation of amplex red and the reductive *N*-deoxygenation of resazurin.

Figure S2 shows in situ UV-Vis absorption spectra of the Pt-nanoparticle-catalyzed oxidative *N*-deacetylation of amplex red by H_2O_2 . The solution was maintained at pH 7.5 using 50 mM phosphate buffer. Over time the absorption bands of resorufin at ~ 572 nm and ~ 295 nm increase in intensity, while that of amplex red at ~ 275 nm decreases, indicating the conversion of amplex red to resorufin (Figure S2A). The clear isosbestic points indicate the quantitative conversion of amplex red to resorufin catalyzed by Pt nanoparticles (Figure 2A, inset). The time profiles of absorption at 275, 295, and 572 nm show the direct correlation between amplex red consumption and resorufin production (Figure S2B, C). As a control, in the absence of Pt nanoparticles, no production of resorufin was observed, in contrast to that in the presence of Pt nanoparticles (Figure 2D, red points versus black points). Besides H_2O_2 , we found that oxygen in air can also act as the oxidant for the oxidative *N*-deacetylation of amplex red in the absence of H_2O_2 (Figure 2D, green point). When amplex red was introduced to the degassed buffer without H_2O_2 , the amount of produced resorufin was significantly decreased (Figure 2D, blue point); the residual resorufin production here was likely due to presence of residual O_2 in the buffer as experiments were not strictly anaerobic. As the concentration of H_2O_2 can be easily controlled, we used H_2O_2 as the oxidant in our single-molecule catalysis experiments.

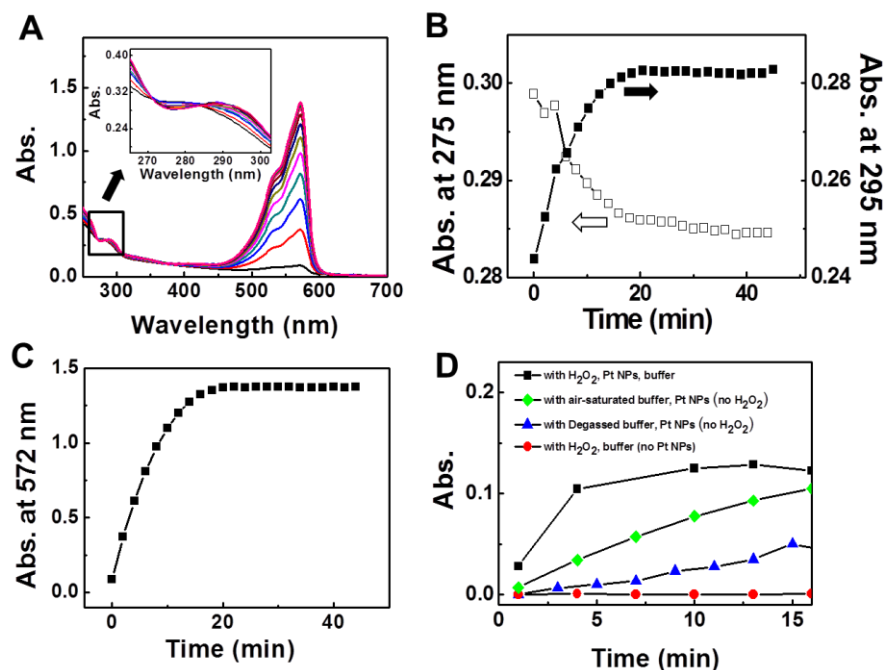


Figure S2. (A) In situ UV-Vis absorption spectra of Pt-nanoparticle-catalyzed oxidative *N*-deacetylation reaction using 200 mM H_2O_2 , 16.7 μM amplex red, ~ 0.02 μM Pt nanoparticles. Spectra were taken at 2 min time intervals. The inset is the magnified spectra in the range from 265 to 305 nm. (B) Time profiles of absorbances at 275 nm and 295 nm, corresponding to the absorption bands of amplex red and resorufin, respectively, from (A). (C) Time profile of absorbance at 572 nm corresponding to the absorption of resorufin from (A). (D) Time profiles

of UV-Vis absorbance at 572 nm (the absorption feature of resorufin) in the presence and absence of $\sim 0.02 \mu\text{M}$ Pt nanoparticles, H_2O_2 and oxygen during the oxidative *N*-deacetylation reaction; [amplex red] = $1.7 \mu\text{M}$, $[\text{H}_2\text{O}_2] = 200 \text{ mM}$. 50 mM pH 7.5 phosphate buffer was used in all ensemble measurements.

Similarly, for the Pt-nanoparticle-catalyzed reductive *N*-deoxygenation of resazurin by N_2H_4 , we monitored the resazurin consumption by its absorption band at $\sim 602 \text{ nm}$ and resorufin production by its absorption band at $\sim 572 \text{ nm}$. Over time the absorption of resorufin increases, while that of resazurin decreases (Figure S3A, B). A clear isosbestic point was observed, indicating the clean conversion of resazurin to resorufin (Figure S3A). As controls, in the absence of N_2H_4 or Pt nanoparticles, no consumption of resazurin (or production of resorufin) was observed (Figure 3C).

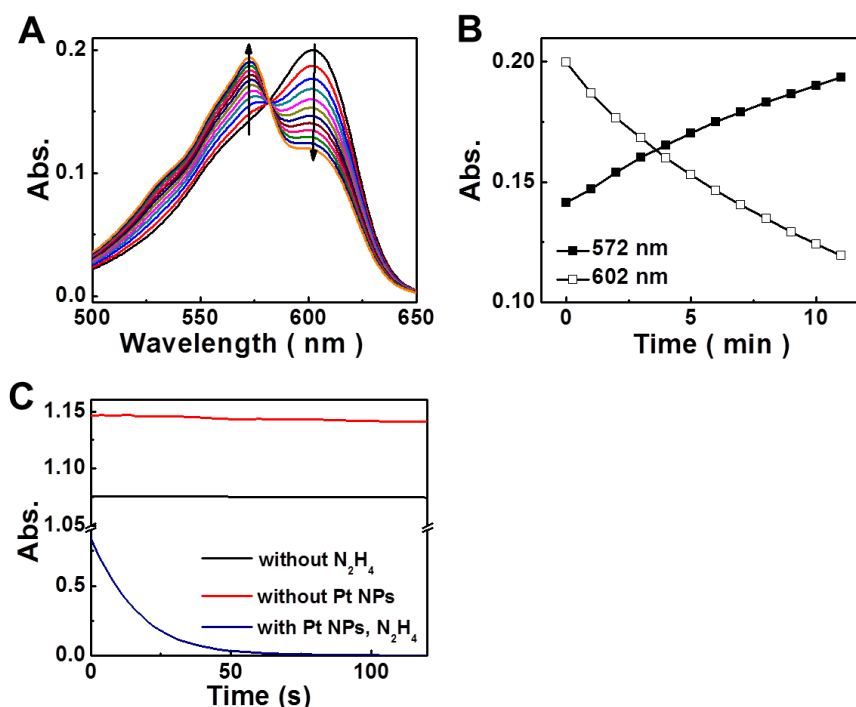


Figure S3. (A) In situ UV-Vis absorption spectra of Pt-nanoparticle-catalyzed reductive *N*-deoxygenation reaction using 1 mM N_2H_4 , 3.6 μM resazurin, $\sim 0.05 \text{ nM}$ Pt nanoparticles. Spectra were taken at 1 min time intervals. (B) Time profiles of UV-Vis absorption at 572 nm and 602 nm, corresponding to the absorption bands of resorufin and resazurin, respectively, from (A). (C) Time profiles of UV-Vis absorption spectra of resazurin at 602 nm in the presence and absence of 1 nM Pt nanoparticles and 1 mM N_2H_4 during the reductive *N*-deoxygenation reaction; [Resazurin] $\approx 20 \mu\text{M}$.

We further investigated the catalytic kinetics of the oxidative *N*-deacetylation reaction and the reductive *N*-deoxygenation reaction at the ensemble level.

For the oxidative *N*-deacetylation reaction, the initial reaction rate (i.e., the initial rate of product formation) shows saturation kinetics with increasing concentrations of either amplex red or H_2O_2 (Figure S4A and B), consistent with the single-molecule measurements of single Pt nanoparticle catalysis (Figure 2A). However, when the reaction rate is normalized by the concentration of Pt nanoparticles, it showed a dependence on the Pt nanoparticle concentration (Figure S6A), whereas

Langmuir-Hinshelwood kinetics predicts it to be independent of Pt nanoparticle concentration. This dependence indicates that there are particle-particle interactions contributing to the catalytic kinetics. These particle-particle interactions are unavoidable in ensemble solution measurements but are cleanly avoided in our single-nanoparticle catalysis measurements, where the nanoparticles are immobilized and spatially separated from each other. These particle-particle interactions in ensemble kinetics likely contribute to the differences between the kinetic parameters obtained from ensemble measurements (Figure S4, caption) and those from single-nanoparticle measurements (Figure 2A).

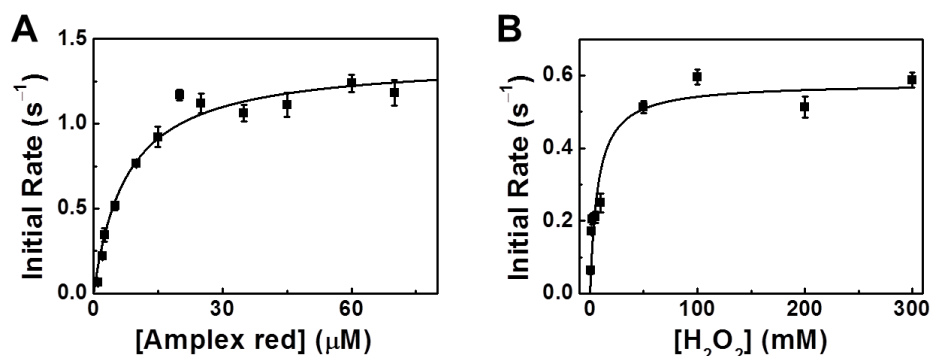


Figure S4. Ensemble catalytic kinetics of Pt-nanoparticle-catalyzed oxidative *N*-deacetylation of amplex red to resorufin by H₂O₂. (A) Amplex red concentration titration of the initial reaction rate at [H₂O₂] = 200 mM and [Pt NPs] ~ 0.02 μM. (B) H₂O₂ concentration titration of the initial reaction rate at [amplex red] = 10 μM, [Pt NPs] ~ 0.02 μM. Initial reaction rate is defined as the production rate of the reaction product resorufin. The solid lines are global fits using $v = kK_{AR}K_O[AR][O]/(1+K_{AR}[AR])(1+K_O[O])$ with $k = 1.38 \pm 0.14 \text{ s}^{-1}$, $K_{AR} = 0.13 \pm 0.05 \text{ μM}^{-1}$ and $K_O = 0.00018 \pm 0.00011 \text{ μM}^{-1}$.

For the reductive *N*-deoxygenation reaction, at a fixed N₂H₄ concentration, the initial reaction rate shows an increase with increasing resazurin concentration and then decays after reaching a maximum (Figure S5A and S5C), consistent with single-nanoparticle catalysis measurements (Figure 2B). On the other hand, when the resazurin concentration is fixed and the N₂H₄ concentration is titrated, the catalytic kinetics can exhibit qualitatively different behaviors depending on the Pt nanoparticle concentration: it can have an initial-increase-followed-by-decay behavior with increasing N₂H₄ concentration (Figure S5B), or simply decay (Figure S5D). When the concentrations of resazurin and N₂H₄ are both fixed, the initial reaction rate, normalized by the Pt nanoparticle concentration, depends *significantly* on the Pt nanoparticle concentration (Figure S6B), indicating significant particle-particle interactions in the ensemble solution catalytic kinetics. All these behaviors reflect the complexity of catalytic kinetics in an ensemble solution reaction. *In contrast, our single-nanoparticle kinetics behaves in a way well described by the classic Langmuir-Hinshelwood kinetics (Figure 2B), in which particle-particle interactions are completely avoided, so we could cleanly measure the kinetics of individual particles.*

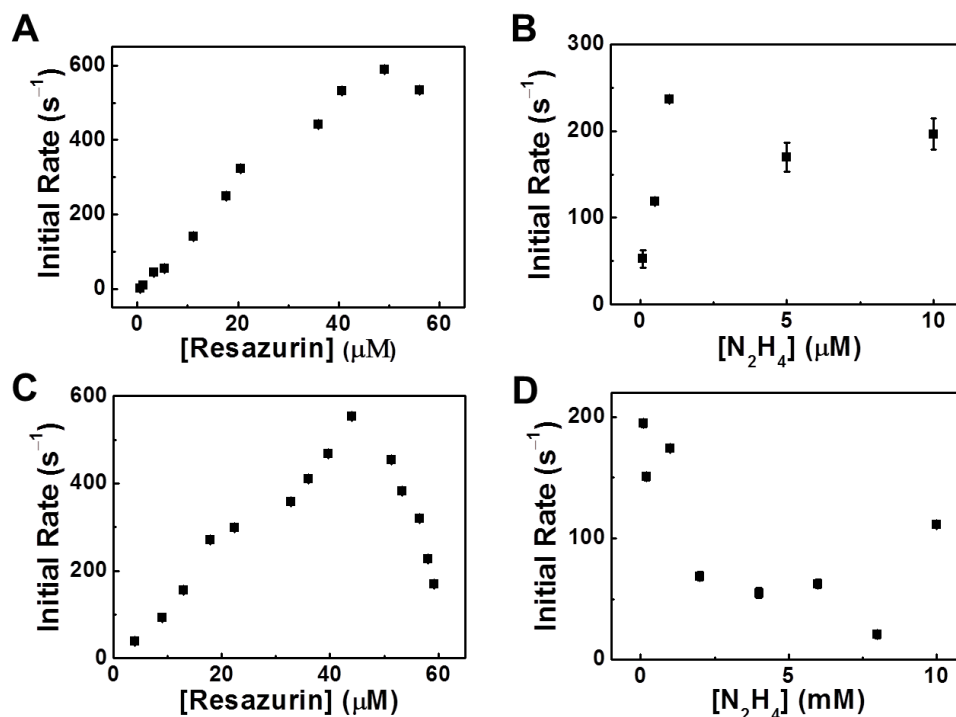


Figure S5. Ensemble catalytic kinetics of Pt-nanoparticle-catalyzed reductive *N*-deoxygenation of resazurin to resorufin by N₂H₄. (A) Resazurin concentration titration of the initial reaction rate at [N₂H₄] = 1 mM, [Pt NPs] ~0.15 nM. (B) N₂H₄ concentration titration of the initial reaction rate at [resazurin] = 20 μM, [Pt NPs] ~0.15 nM. (C) Resazurin concentration titration of the initial reaction rate at [N₂H₄] = 1 mM, [Pt NPs] = 0.05 nM. (D) N₂H₄ concentration titration of the initial reaction rate at [resazurin] = 20 μM, [Pt NPs] = 0.05 nM. Initial reaction rate is defined as the production rate of the reaction product resorufin.

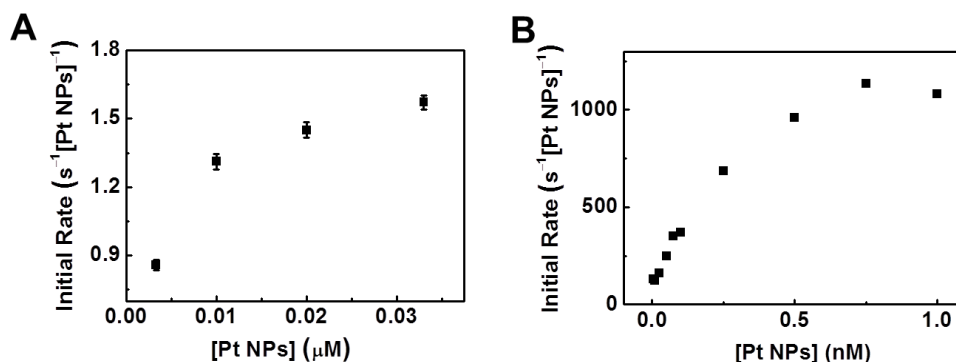


Figure S6. Dependence of the initial reaction rate on the concentration of Pt nanoparticles for (A) the oxidative *N*-deacetylation reaction ([H₂O₂] = 200 mM, [AR] = 20 μM) and (B) the reductive *N*-deoxygenation reaction ([N₂H₄] = 1 mM, [RZ] = 40 μM). The initial reaction rates here are normalized by Pt nanoparticle concentration.

4. Dependences of the activity fluctuation rate on the single-particle turnover rate of Au nanoparticles in catalysis

In our previous study of single 6–14 nm Au nanoparticles in catalyzing the reductive *N*-deoxygenation of resazurin,^{3,4} we observed temporal activity fluctuations of individual Au nanoparticles

under steady state reaction conditions, which are attributable to catalysis-induced and spontaneous dynamic surface restructuring. The timescale of the underlying dynamic surface restructuring is obtainable from the autocorrelation function of the microscopic reaction time (as in Figure 3 in the main text), and it shows a dependence on both the single-particle turnover rate and the nanoparticle size. The rate of the activity fluctuations (and thus the underlying dynamic surface restructuring) increases linearly with increasing turnover rate, reflecting the catalysis-induced contributions. The extrapolation of activity fluctuation rate to zero turnover rate approximates the rate of spontaneous dynamic surface restructuring, which becomes faster with decreasing size, reflecting, as well as being consistent with, the less stable surfaces of smaller nanoparticles. We formulated a simple thermodynamic model to analyze quantitatively the catalysis- and size-dependent dynamic surface restructuring of Au-nanoparticles. In this model, we assumed: (1) a linear relation between r , the rate of dynamic surface restructuring of the nanoparticle, and ν , its rate of turnovers, as observed experimentally; (2) the activation energy of spontaneous dynamic surface restructuring is proportional to the cohesive energy $E(d)$ of the nanoparticle, which is well known to depend on the particle diameter d .⁵⁻⁷ This simple model gives

$$r = r_{\text{sp}}^0 \exp(-\beta E(d) / RT)(1 + q\nu) \quad (\text{S20})$$

Here r_{sp}^0 is the rate of spontaneous dynamic surface restructuring when thermal energy is much larger than the activation energy; β is a proportionality constant connecting the activation energy of spontaneous dynamic surface restructuring to the cohesive energy of the nanoparticle $E(d)$; and q is a proportionality constant reflecting the linear coupling between the rate of the dynamic surface restructuring r and the turnover rate ν . R is the gas constant, and T is temperature. This model fits satisfactorily the results of Au nanoparticles of varying diameters,^{3,4} giving $r_{\text{sp}}^0 = 20 \pm 18 \text{ s}^{-1}$, $\beta = 0.061 \pm 0.006$, and $q = 32 \pm 9 \text{ s}$ (note the value of q here is an average of the two values for the catalytic product generation reaction and the product dissociation reaction, which were separately analyzed for the Au nanoparticles; please see reference^{3,4} for details). Using Equation (S20) and fitted parameters for Au nanoparticles, the derived dependence of r on ν for Au nanoparticles of diameter 4.6 nm is plotted in Figure 3C in the main text.

5. Product identification and reaction stoichiometry of Pt-nanoparticle-catalyzed reactions.

We used proton NMR to identify/confirm the reaction products of the Pt-nanoparticle-catalyzed *N*-deacetylation of amplex red by H_2O_2 . By comparing the proton NMR spectrum of the reaction solution with those of amplex red, resorufin, sodium acetate, we clearly observed that amplex red was oxidized to resorufin and the by-product is acetate (Figure S7C). Proton quantitation from the NMR spectra indicates that the product resorufin and acetate are generated in 1:1 stoichiometry. Using this information, a balanced chemical equation is given in Figure S7A for this oxidative *N*-deacetylation reaction

For the reductive *N*-deoxygenation of resazurin by N_2H_4 , we have not experimentally identified the product from the oxidation of N_2H_4 . Previous experimental⁸⁻¹² and theoretical¹³ studies of hydrazine oxidation showed that nitrogen and water are the main products (for example: $\text{N}_2\text{H}_4 + 2\text{NO} \rightarrow 2\text{N}_2 + 2\text{H}_2\text{O}$), while many intermediates, NH_3 and N_2H_3 or NH_2 , were suggested. Assuming the reaction products from N_2H_4 in our catalysis here are also nitrogen and water, Figure S7B gives a balanced reaction equation as a possibility.

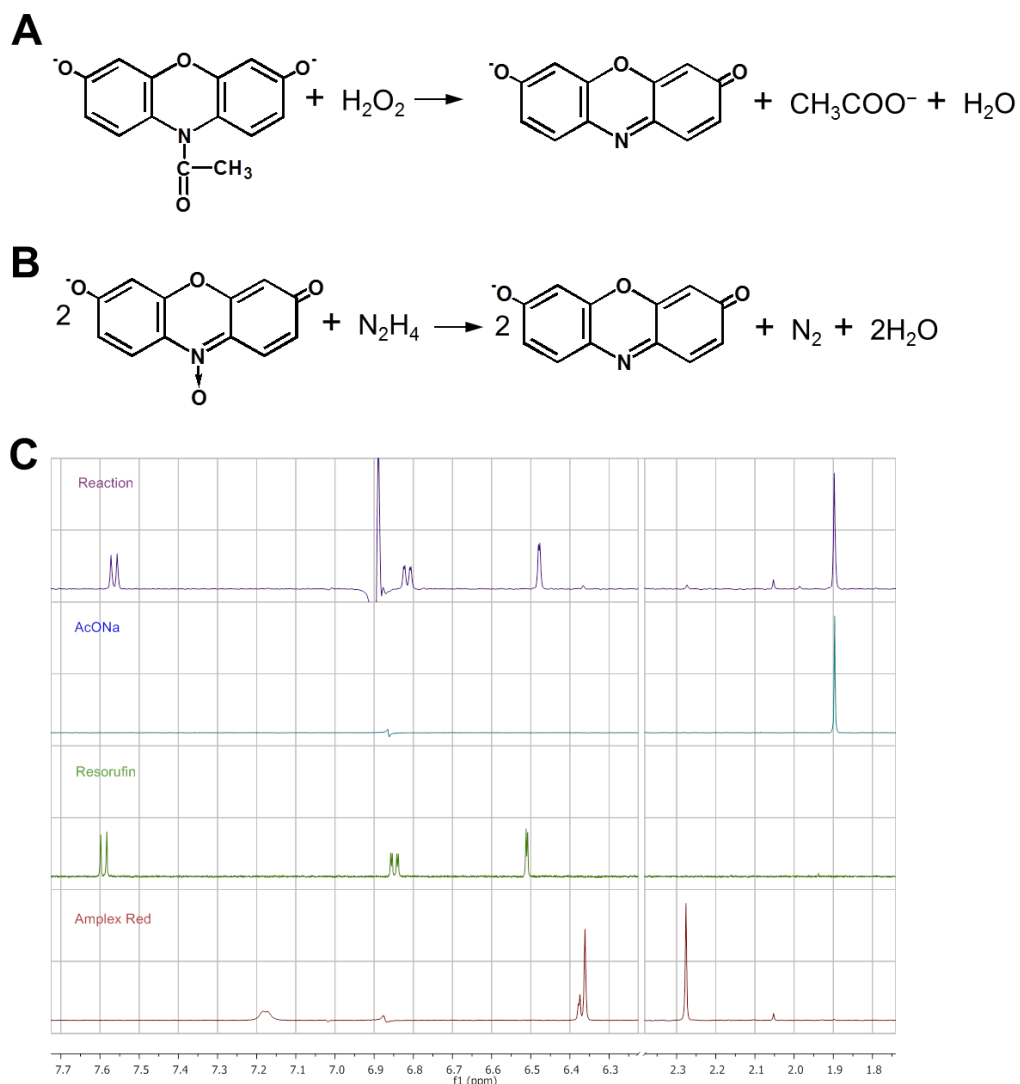


Figure S7. (A) Balanced chemical equation of oxidative *N*-deacetylation of amplex red by H_2O_2 catalyzed by Pt nanoparticles in aqueous solution. (B) One possible balanced chemical equation of reductive *N*-deoxygenation of resazurin by N_2H_4 . (C) NMR spectra of amplex red, resorufin, sodium acetate and the reaction solution of the oxidative *N*-deacetylation reaction of amplex red by H_2O_2 catalyzed by Pt nanoparticles. The large peak at ~ 6.9 ppm in the top spectrum is a quadrature artifact arising from the very intense peak at 2.71 ppm from DMSO used as the internal standard (not shown in the figure).

6. TEM characterization of Pt nanoparticles before and after catalysis

Figure S8 shows the TEM images of Pt nanoparticles before and after the catalytic reactions. Compared with as-synthesized Pt nanoparticles (Figure S8A), the Pt nanoparticles after undergoing the oxidative *N*-deacetylation reaction (Figure S8B) or the reductive *N*-deoxygenation reaction (Figure S8C) do not show large morphology changes, although slight rounding of corners and edges is noticeable.

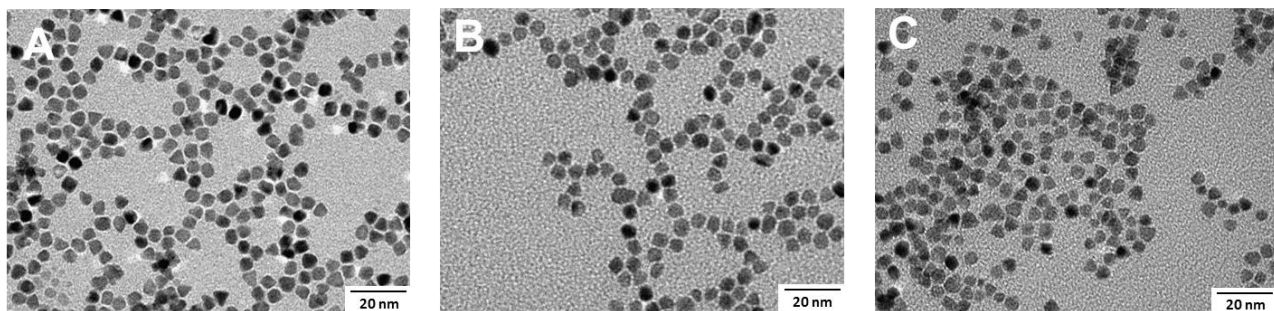


Figure S8. TEM images of (A) as-synthesized Pt nanoparticles, and (B) of those after undergoing the *N*-deacetylation reaction, and (C) of those after undergoing the *N*-deoxygenation reaction.

REFERENCES

- (1) Eychmuller, A.; Bigall, N. C.; Hartling, T.; Klose, M.; Simon, P.; Eng, L. M. *Nano Letters* **2008**, *8*, 4588.
- (2) Satterfield, C. N. *Heterogeneous Catalysis in Practice*; McGraw-Hill Book Company: New York, **1980**.
- (3) Xu, W.; Kong, J. S.; Yeh, Y.-T. E.; Chen, P. *Nature Mater.* **2008**, *7*, 992.
- (4) Zhou, X.; Xu, W.; Liu, G.; Panda, D.; Chen, P. *J. Am. Chem. Soc.* **2010**, *132*, 138.
- (5) Jiang, Q.; Li, J. C.; Chi, B. Q. *Chem. Phys. Lett.* **2002**, *366*, 551.
- (6) Lu, H. M.; Jiang, Q. *J. Phys. Chem. B* **2004**, *108*, 5617.
- (7) Yang, C. C.; Li, S. *Phys. Rev. B* **2007**, *75*, 165413.
- (8) Bamford, C. H. *T Faraday Soc.* **1939**, *35*, 0568.
- (9) Bamford, C. H. *T Faraday Soc.* **1939**, *35*, 1239.
- (10) Gray, P.; Spencer, M. *T Faraday Soc.* **1963**, *59*, 879.
- (11) Glarborg, P.; Damjohansen, K.; Miller, J. A.; Kee, R. J.; Coltrin, M. E. *Int. J. Chem. Kinet.* **1994**, *26*, 421.
- (12) Tuazon, E. C.; Carter, W. P. L.; Winer, A. M.; Pitts, J. N. *Environ. Sci. Technol.* **1981**, *15*, 823.
- (13) Harrison, J. A.; Whyte, A. R.; Phillips, L. F. *Chem. Phys. Lett.* **1986**, *129*, 346.